Research Article | Vol. 9, No. 11 | 1 Nov 2018 | BIOMEDICAL OPTICS EXPRESS 5597
Biomedical Optics EXPRESS

Non-contact dynamic diffuse optical tomography imaging system for evaluating lower extremity vasculature

J. W. Hoi,[1] H. K. Kim,[2] C. J. Fong,[1] L. Zweck,[3] and A. H. Hielscher[1,2,4,*]

[1]*Department of Biomedical Engineering, Columbia University, 351 Engineering Terrace, 500 W. 120th St., New York, NY 10027, USA*
[2]*Department of Radiology, Columbia University, 630 W. 168th St., New York, NY 10032, USA*
[3]*Faculty of Engineering, Friedrich-Alexander-Universität, Martensstraße 5a, 91058 Erlangen, Germany*
[4]*Department of Electrical Engineering, Columbia University, 1300 S.W. Mudd, 500 W. 120th St., New York, NY 10027, USA*
**ahh2004@columbia.edu*

Abstract: A novel multi-view non-contact dynamic diffuse optical tomographic imaging system for the clinical evaluation of vasculature in the lower extremities is presented. The system design and implementation are described in detail, including methods for simultaneously obtaining and reconstructing diffusely reflected and transmitted light using a system of mirrors and a single CCD camera. The system and its performance using numeric simulations and optical phantoms. Measurements of a healthy foot in vivo demonstrates the potential of the system in assessing perfusion within the foot.

1. Introduction

Over the last decade, diffuse optical imaging (DOI) systems have been developed for clinical applications such as breast cancer [1–5], arthritis [6–8], brain function [9, 10], and vascular diseases [11–13]. This can be attributed to DOI's ability to non-invasively measure functionally relevant parameters. Diffuse optical measurements are mostly based on the wavelength dependent intrinsic absorption contrast of oxyhemoglobin (HbO_2) and deoxyhemoglobin (Hb). This makes dynamic diffuse optical tomography (DDOT) well suited for imaging peripheral arterial disease (PAD), a disease in which narrowed or blocked arteries results in reduced blood flow to the lower extremities. Untreated or unsuccessful treatment of the disease eventually leads to foot ulcers, open wounds, gangrene, and amputation. Patients require frequent evaluation to monitor the disease progression [14], but current methods of evaluating PAD do not directly measure the perfusion in the foot where tissue death commonly begins. Current methods are also often inconclusive or contraindicated in patients with diabetes and renal insufficiencies [15–17], who account for up to 41% of PAD patients [18]. Evaluation of PAD in this population is hampered by the lack of a non-ionizing and contrast-free method to assess the blood perfusion in the distal portions of the lower extremities.

We have previously shown that DDOT has great potential for detecting PAD by extracting time-dependent features of the total hemoglobin concentrations in the foot during a venous occlusion at the thigh [11, 12]. The venous occlusion blocks blood from returning to the heart while the blood continues to flow through the arteries to the lower leg. The hemodynamics during the occlusion reveals information about the arterial vasculature and perfusion. Furthermore, the angiosome concept has found increasing attention in the vascular surgery community. It is thought that different volumes of tissue in the foot, or angiosomes, each has its blood supplied by a specific more proximal artery [19]. Recent studies have shown that direct revascularizations of the arteries tied to specific angiosomes affected by

#340004 https://doi.org/10.1364/BOE.9.005597
Journal © 2018 Received 17 Jul 2018; revised 26 Aug 2018; accepted 27 Aug 2018; published 19 Oct 2018

Biomedical Optics EXPRESS

PAD leads to a higher rate of healing and limb salvage [20–22]. The ability to evaluate the areas of the foot with low perfusion would be useful. Here, the tomographic capabilities of DDOT could play an important role.

Like many other traditional DDOT imaging systems, our previous system employed optical fibers in direct contact with the tissue surface to deliver and collect light [11, 12]. We found that this limits its clinical utility, especially in patients with open wounds and ulcers, which is a common occurrence in PAD patients. In these patients, fibers need to be placed outside the wound, further complicating an already cumbersome and time-consuming process. In general, establishing proper fiber-skin contact is difficult, but important for obtaining quality data. Furthermore, the number of the fibers that can be used is limited by the size of the fibers themselves. This in turn limits the number of data points that can be collected. In addition, the bulk of the fibers around the imaged object makes it difficult to recover the object geometries and the fiber positions, which is important for an accurate image reconstruction process. For all these reasons, it is highly desirable to have a non-contact DDOT system for the assessment of PAD in the feet of affected patients.

Recently, fiber-less non-contact systems have emerged in the field of small animal imaging [23, 24]. In these system, wide-field CCD or CMOS sensors are utilized which allows for higher spatial resolution of detection points from the tissue surface and avoids the placement issues of fibers. Furthermore, the geometry of the object can be more easily extracted. Continuous-wave (CW) DOT systems allow for fast frame-rates, making it ideal for dynamic imaging. Adapting these small-animal imaging systems for human clinical use is non-trivial. Systems geared for clinical use largely employ a single view mode. These systems use reflectance only to measure oxygen saturation in the skin and muscle. Transmission only noncontact systems have been developed for hand and finger imaging [7].

Here, we have developed a multi-view non-contact dynamic diffuse optical tomography system for imaging the blood flow in the foot using a mirror-based scheme. The system's ability to resolve inhomogeneity was characterized using numeric simulations and tissue mimicking phantoms with high absorbing inclusions. The system was also tested on a healthy foot during a venous occlusion and was able to provide spatial maps of hemodynamic changes. From these time-varying maps, we can extract functional information about the lower extremity vasculature, which may be very useful in evaluating diseases such as PAD.

2. System design

We designed a novel non-contact multi-view CW DDOT system to image the hemodynamics of the mid-metatarsal level of the foot. PAD patients often develop ulcers in this area of the foot and DDOT measurements there can differentiate between healthy and PAD patients [11, 12]. The overall schematic of the system is depicted in Fig. 1. A seated patient places his or her foot inside the imager on an angled platform with an open rectangular window. The foot is illuminated from above while a camera, also above the foot, directly captures diffusely reflected light. Transmitted light is simultaneously reflected to the same camera by a system of mirrors. The foot is held in place laterally from both sides by padded blocks. These padded blocks slide in from each the side of the foot and lock into place. In this way, the foot is able to rest on the platform to remain stable and limit motion artifacts during imaging.

With this overall design, the DDOT system can be broken down into five units: the (1) input unit, (2) imaging head, (3) detection unit, (4) control unit, and (5) surface scanner. The input unit delivers CW source point illuminations to the top of the foot. The imaging head projects light re-emitted from the foot to the detection unit. The detection unit captures the re-emitted light from the top and bottom of the foot. The control unit manages the imaging sequences. Finally, the surface scanner obtains the dorsal foot geometry. Each unit is described in detail below.

Biomedical Optics EXPRESS

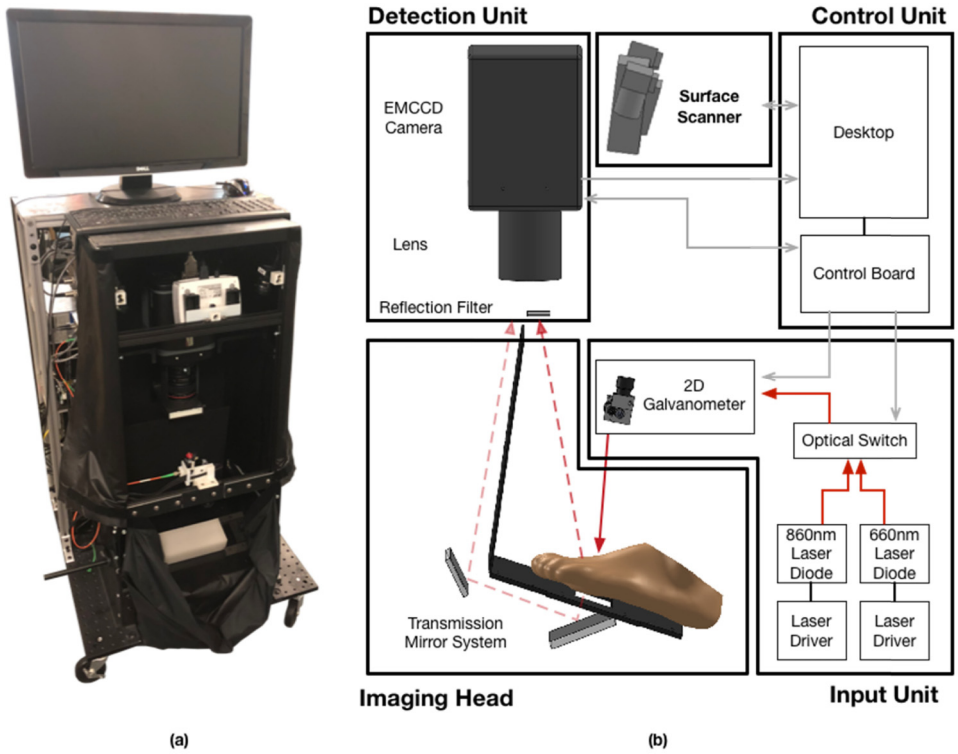

Fig. 1. (a) Photograph and (b) block diagram of the imaging system.

2.1 Input unit

The main components of the input unit are two 350mW laser diodes with built-in thermoelectric control (660nm and 860nm, Intense Inc., USA). These diodes are driven by two laser drivers (ITC102, Thorlabs Inc., USA) in constant-current mode to provide constant CW light. The two wavelengths are time-series multiplexed onto a single graded-index multimode fiber patch cable (62.5µm core, 1m length, FC/APC connectors, Thorlabs Inc., USA) using an optical MEMS switch (Leoni AG, Germany).

The light from the patch cable is collimated (F240APC-780, Thorlabs Inc., USA) to a spot size with a diameter of ~2mm. The collimated light is coupled with a 2D galvanometer scanner (12.5° x 12.5° scanning angle, GVSM002-Silver, Thorlabs Inc., USA) placed approximately 25cm above the platform. The galvanometer deflects the collimated light to the top of the foot to provide multiple source point illuminations with a resolution of 0.0008°. The laser intensity is tuned to deliver approximately 30mW and 40mW to the foot for the 860nm and 660nm wavelengths, respectively.

The source illumination point coordinates are needed to reconstruct the optical properties within the foot. In this system, the 2D galvanometer scanner deflects the laser beam via the rotation of two perpendicular mirrors. The rotations of the mirrors control the horizontal X-axis and vertical Y-axis beam deflection to any position within the two dimensions, sometimes referred to as the marking field. However, the use of a two-mirror deflection system leads to geometric distortions in the marking field. For example, scanning the laser in a square-shaped pattern on a planar surface will produce a pin-cushion pattern [25, 26]. Additional geometric distortions are caused by misalignments of the incoming laser beam [27]. To characterize these geometric distortions, we map the marking field in 3D using calibration measurements from the galvanometer scanner.

Biomedical Optics EXPRESS

We acquire images of a 12x12 grid pattern of (X, Y) laser beam deflection from the galvanometer scanner onto a planar platform using the built-in camera at 8 known vertical heights within the system, resulting in 1152 images. Each of these images captures the laser point and a calibration pattern printed on the platform. The images are scaled and co-registered to a physical dimension coordinate system based on known dimensions in the camera calibration pattern and the vertical positions of the platform within the system.

Once the images are in a 3D coordinate system, the coordinate of the laser point in each image is extracted. A line through all of the coordinates obtained for one (X, Y) rotation pair represents the light beam path from the galvanometer scanner. A combination of these lines for different (X, Y) rotation pairs forms a 3D marking field that characterizes the geometric distortions. This 3D marking field is co-registered with the mesh using the coordinates of the four corners of the rectangular transmission window. This co-registered 3D marking field is shown in yellow in Fig. 2(a).

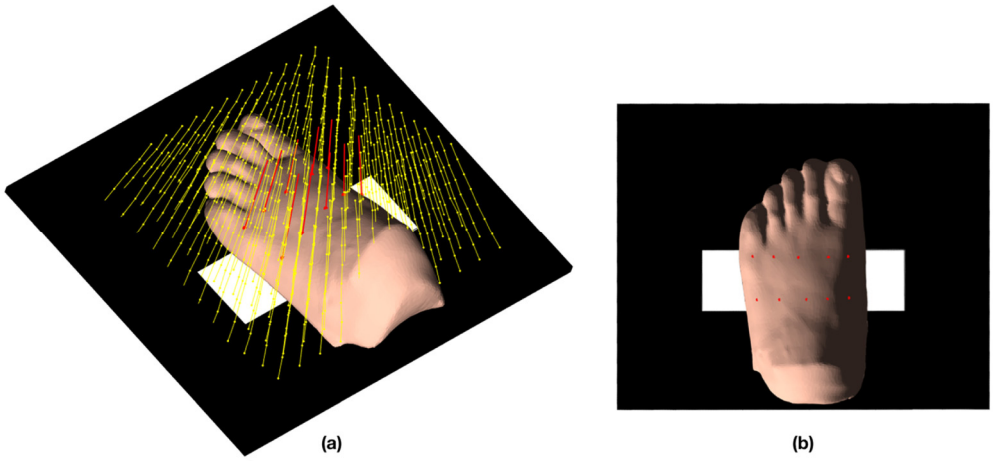

Fig. 2. (a) Co-registered galvanometer scanner marking field (yellow) and interpolated laser paths (red) for ten source positions. (b) Extracted source positions (red) on the foot mesh.

The location of the source illumination point on the foot is extracted by first interpolating the laser path for the (X, Y) mirror rotations, shown in red in Fig. 2(a). Then, the point of intersection of the laser path and the mesh is the source illumination point. The resulting source points on the mesh are displayed as red dots in Fig. 2(b). The marking field only needs to be generated once, assuming the components remain fixed relative to each other. This method was verified by comparing extracted source positions to 20 known locations on a block phantom. The maximum error between the actual position and the extracted position was <0.5mm.

2.2 Imaging head

The imaging head simultaneously projects back-reflected light from the top of the foot and transmitted light from the bottom of the foot to the detection unit. The back-reflected light is directly captured by the camera sensor, while transmitted light from the bottom of the foot is captured through a system of two protected silver coated mirrors (Nu-Tek Precision Optical Corp., USA), as depicted in Fig. 1. The foot platform has a transmission window 2in ($\overline{DE}$) by 6in in size. Figure 3(a) and Table 1 show the parameters for positioning the components in the imaging head. This configuration results in an optical path length difference between the reflection and transmission light of ~8in and has a SNR of ~16dB through the system of mirrors. The resulting raw camera image simultaneously captures the top and bottom of the foot in Fig. 3(b).

Biomedical Optics EXPRESS

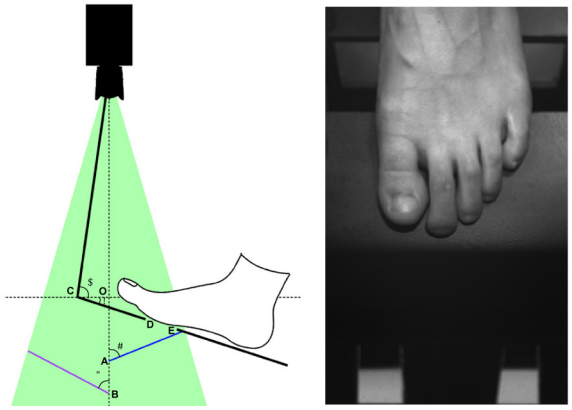

Fig. 3. (a) Schematic of parameters defining the imaging head. (b) Raw camera image of a foot. The top portion of the image shows the top of the foot, while the bottom portion of the image shows a portion of the bottom of the foot through the transmission window.

Table 1. System Parameters for Fig. 3(a)

$\overline{CD}$	$\overline{DE}$	$\overline{AO}$	$\overline{BO}$	α	β	ε	γ
4.5 in.	2 in.	4 in.	7 in.	68°	27°	18°	81.9°

2.3 Detection unit

A back-illuminated electron multiplying charge coupled device (EMCCD) camera (ProEM 512B-EX, Princeton Instruments, USA) captures the diffusely reflected and transmitted light from the foot. The camera sensor has an 8.2x8.2mm imaging area (16μm x 16μm pixel size, 512x512 pixel resolution) that coupled with a lens (14mm f/2.8, Canon, USA) results in a 32.6° angle of view. The lens is operated at its maximum aperture of f/2.8 to maximize the light collected from the transmission signal. This aperture results in a narrow focal depth, which is manually focused to the focal plane between the top and bottom of the foot. The EMCCD acts as a fiber-free wide field detector with a spatial resolution of approximately 2.5px/mm in the reflection geometry and 1.5px/mm in the transmission geometry. For imaging the foot, we utilize a 312x512 pixel portion of the CCD without binning. A narrower region of the sensor is used since the foot is generally not wider than the 6in width of the transmission window. These settings result in a readout time of approximately 60ms.

The EMCCD is air cooled to −70°C for low light sensitivity, with approximately 95% quantum efficiency at 860nm. The camera has a dynamic range of 16-bits (96dB). However, to capture both low transmission signals and high reflection signals simultaneously with a single CCD sensor, the reflected light must be attenuated. Photons emitted from the top of the foot pass through a fixed position neutral density filter before entering the camera-lens system. This ensures the reflected signals do not saturate the CCD. The neutral density filters have an optical density of 1.8 for the 860nm wavelength and 1.95 for the 660nm wavelength. Additional black out filters are used to prevent detection and saturation from source illumination reflections, allowing for better use of the camera's dynamic range. Strips of high absorbing blackout tape (<1e-5% transmittance @ 850nm, T205-2.0, Thorlabs Inc., USA) are secured in front of the portion of the lens capturing the reflected light. These strips are placed such that they block strips of view of the top of the foot. The source positions can then be positioned on the top of the foot such that they align with the camera's blocked view of the foot. Thus, any specular reflections are blocked from being detected by the camera sensor by the blackout tape.

Biomedical Optics EXPRESS

2.4 Control unit and data acquisition

A Matlab graphical user interface (GUI) on a desktop computer provides an interface to control the imaging procedure. First, the user selects the source positions for an imaging acquisition. The source illumination points must be selected for each acquisition since the geometry of each foot is different and the source points should align with the fixed position filters. The list of source positions and length of the acquisition indicated in the GUI are sent to the control board via serial communication. The camera's WinX software (Princeton Instruments, USA) is used to initialize the camera settings and collect the CCD images in external triggering mode. Once data acquisition is started, the control board manages and synchronizes the switch, galvanometer, and camera triggering. The switch is controlled by 4 TTL signals. The galvanometer scanner is controlled by two differential analog signals (−10V to 10V). The camera is triggered by the rising edge of a short TTL pulse.

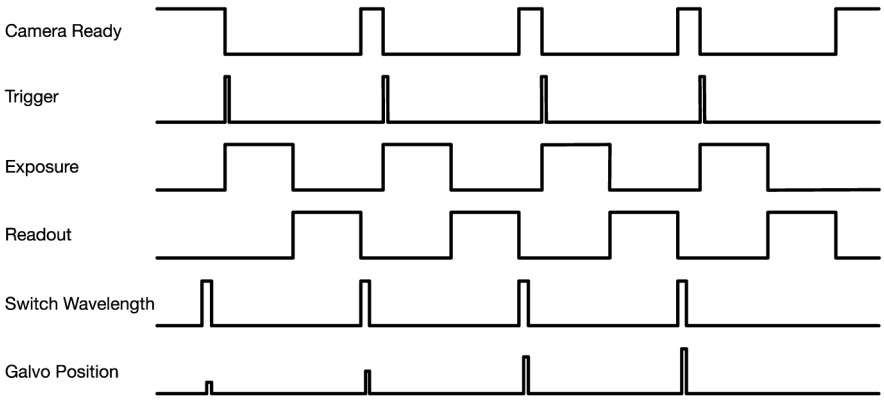

Fig. 4. Control board timing diagram for a data acquisition sequence.

The timing diagram for an imaging sequence is shown in Fig. 4. When the camera is ready, the control board signals the switch to change wavelength, sets the source position via the galvanometer, and then triggers the camera to collect an exposure. The control board waits for the camera to finish the exposure and readout, and then repeats the process until the indicated number of frames is captured.

2.5 Surface scanner

The surface geometry of the foot is necessary for image reconstruction of the hemodynamic properties within the foot. The surface information is captured with an integrated structured light surface scanner (SLS-2, David Vision Systems, Germany), comprised of a white light projector and two cameras. These components are placed above the foot outside the EMCCD's field of view (FOV). The galvanometer is above the foot for data acquisition, but it can be slid out of the FOV of the surface scanner to obtain the foot geometry. The surface scanner projects sinusoidal light patterns onto the foot while the cameras capture the reflection of the disrupted patterns. These disruptions are used to create 3D point clouds and a surface mesh. The two cameras capture two different views of the imaged object, ensuring that the entire dorsal surface of the foot is captured. The scanning process takes less than one minute (26 seconds per camera scan using 58 patterns and texture).

The two scans are fused in the David software with a flat bottom to create a closed surface mesh. The surface mesh is converted to a volume mesh using MeshLab and Gmsh. The local coordinates of the volume mesh are translated into the global coordinates of the system based on the coordinates of the four corners of the transmission window, which are also captured during the surface scan. The scanned foot platform is shown in blue with a grey foot mesh in

Biomedical Optics EXPRESS

Fig. 5(b). This setup allows the surface geometry to be obtained within the system, enabling better co-registration.

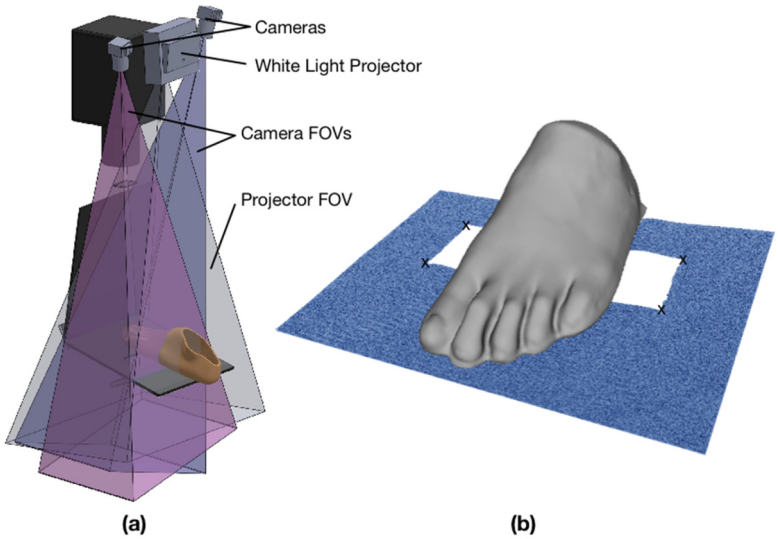

Fig. 5. (a) CAD drawing of the surface scanner and fields of views of the cameras and the projector. (b) Resulting scan of the foot mesh and the transmission window.

3. Image reconstruction

3.1 Measurement operator

In non-contact camera-based systems, only a portion of the photons emitted from the tissue surface is captured by the camera sensor, as illustrated in Fig. 6(a). The amount of light that reaches the camera sensor depends upon the surface radiation from the tissue and the specific setup of the camera system. Therefore, an accurate ray transfer model from the object space to the camera sensor plane is crucial for quality image reconstruction. The measurement operator provides a mapping of the spatial distribution of emitted light from the tissue surface onto the detectors of the camera and can be defined as:

$$z(\vec{r}_D) = Q\psi(\vec{r}_O, \vec{s}) \tag{1}$$

where $z(\vec{r}_D)$ is the amount of light measured at detector (sensor) location $\vec{r}_D$, $\psi(\vec{r}_O, \vec{s})$ is the light intensity emitted at object surface $\vec{r}_O$ in direction $\vec{s}$, and Q is the measurement operator that projects the object radiation $\psi(\vec{r}_O, \vec{s})$ onto the sensor plane to create an image of $z(\vec{r}_D)$. A raw camera image of a foot phantom is shown in Fig. 6(b) with the corresponding binary image of mapped pixels from the measurement operator.

If the imaging plane is in focus, the sensor plane is the same as the imaging plane. However, the sensor plane is offset from the imaging plane in this system, causing a slight blurring of both surfaces (see Fig. 6(b)). Knowing the camera parameters (e.g. the object distance, image distance, and sensor distance), the ray tracing can account for the mismatch between the image plane and the sensor plane. Thus, each pixel of the sensor plane image is a weighted sum of the emitted rays from different points on the surface of the foot, effectively providing a weighted average. The measurement operator is the inverse of this mapping such that when applied to the detection values at each pixel, we solve for the radiance at each point on the surface. Then, these radiance values are used to reconstruct the hemoglobin concentrations within the foot. More details on the procedure for constructing the measurement operator Q can be found elsewhere [24, 28].

Biomedical Optics EXPRESS

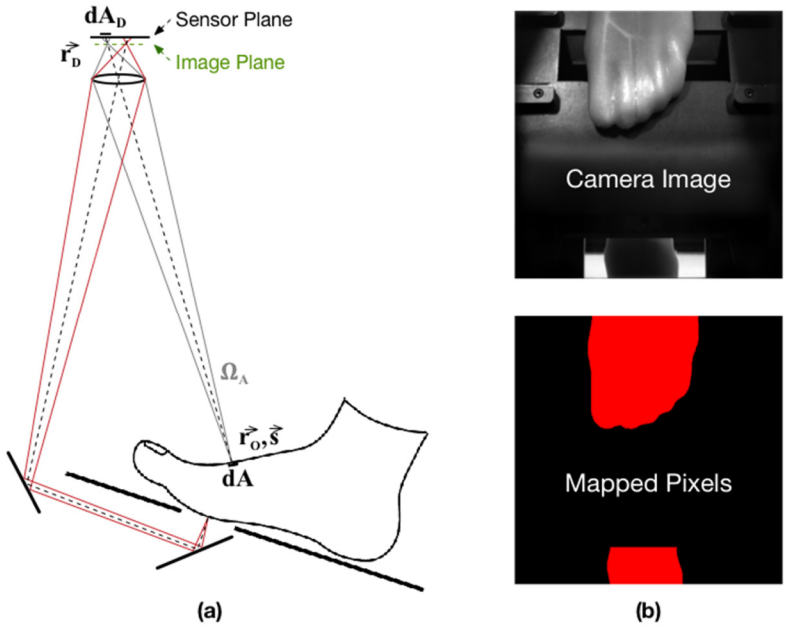

Fig. 6. (a) Measurement operator mapping from the foot surface to the sensor plane. (b) Raw camera image and binary image of mapped pixels by the measurement operator.

3.2 Reconstruction

The camera detector readings z_d calculated from the measurement operator as given in Eq. (1) are directly reconstructed into 3D maps of chromophore concentrations $c(x, y, z)$ using a diffusion approximation based multispectral reconstruction algorithm [29-31]. This algorithm makes use of a discrete cosine transformation (DCT) based neural network approach within a framework of PDE-constrained optimization. The algorithm reconstructs the relative changes from difference data between the target and reference by minimizing an objective function $f(c)$ that describes a mismatch between predictions $Q\psi_{d,\lambda}$ and measurements $z_{d,\lambda}$ of light intensities on the camera sensors, given by:

$$f\big(c(x,y,z)\big) = \sum_{d,\lambda}\big(Q\psi_{d,\lambda} - z_{d,\lambda}\big)^2. \tag{2}$$

In vascular imaging, we are mainly interested in recovering image contrast based on absorption. Thus, the scattering is assumed to be homogenous throughout the imaged object. We also assume homogenous concentrations of HbO_2 and Hb to generate the forward prediction for the baseline reference state. The ratio of the target data to the reference data scales the reference state forward prediction model. The reconstructed values from this normalized data represent the difference in percent change relative to the reference state.

To quantify the quality of the reconstructions, we use the correlation factor (ρ) and deviation factor (δ). The correlation factor indicates the degree of structural similarity between the exact and reconstructed images and ranges from -1 to 1. The deviation factor describes the discrepancy in the absolute values of exact and reconstructed quantities. The closer the correlation factor gets to 1, and the closer the deviation factor gets to 0, the more accurate the reconstruction. Where $\bar{c}$ and $\sigma(c)$ are the mean and standard deviations of the absorption coefficient observed spatially, the correlation and deviation factors are defined as:

Biomedical Optics EXPRESS

$$\rho\left(c^e,c^r\right)=\frac{\sum_{i=1}^{N}\left(c_i^e-\bar{c}^e\right)\left(c_i^r-\bar{c}^r\right)}{\left(N-1\right)\sigma\left(c^e\right)\sigma\left(c^r\right)} \tag{3}$$

$$\delta\left(c^e,c^r\right)=\frac{\sqrt{\sum_{i=1}^{N}\left(c_i^e-c_i^r\right)^2/N}}{\sigma\left(c^e\right)} \tag{4}$$

4. System characterization and performance

4.1 Dark noise and dynamic range

The 16-bit EMCCD has a maximum count level of 65,536. The dark noise count for a 75ms integration time is approximately 654rms for EM gain factors up to 1000x, resulting in an effective dynamic range of 40dB. This increases to 791rms for 300ms integration times (38dB). The background count, which includes the dark noise and ambient light leakage into the system, is 656rms and 792rms for 75ms and 300ms integration times, respectively. This indicates that the ambient light leakage into the system is minimal.

4.2 Detection linearity

To determine the system detection linearity, the EMCCD signal was measured as a function of the laser intensity (within the range between dark noise and saturation) through a solid phantom. This was completed for both wavelengths at an EM gain factor of 50. The system showed good linearity with a R^2 value of 0.999 for both 860nm and 660nm over the dynamic range of the camera (Fig. 7(a) and (b), respectively). Similar results were found for an EM gain factor of 5.

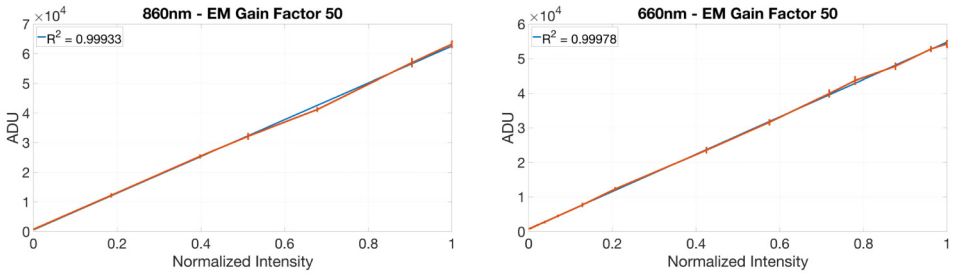

Fig. 7. Detection linearity for (a) 860nm and (b) 660nm at a gain factor of 50.

4.3 Detection stability

Repeated measurements of a solid block phantom with 10 source positions were taken over a 1-hour time interval with the same experimental settings. A 3-minute recording was acquired after the EMCCD reached the cooled temperature, and again at 5 minutes, 10 minutes, 20 minutes, 40 minutes, and 1 hour after the initial recording. The coefficient of variation (CV) was calculated for various detector pixels over the 1-hour time interval. The mean CV was 0.63% for 860nm and 0.88% for 660nm.

4.4 Frame-rate

The system is designed for dynamic imaging of the blood perfusion and the speed of acquisition is important. Since each source position and wavelength is sequentially imaged, the frame-rate is limited by the acquisition time of each exposure and the number of source

Biomedical Optics EXPRESS

positions. The frame-rate decreases with increasing source positions and integration times. The acquisition time for each wavelength at a source position is approximately the integration time plus a 60ms readout time. For 10 source positions, 2 wavelengths, and a 75ms integration time, the frame-rate is approximately 0.33Hz. This is sufficient to capture hemodynamics during a one-minute long venous occlusion.

4.5 Block phantom experiments

A solid block phantom (Fig. 8) was used to determine the system's ability to localize absorbers and to recover varying absorption contrasts. A silicone-based rectangular phantom (16.5cm x 6.4cm x 4.5cm) was fabricated using Sylgard 184 PDMS, titanium dioxide, and India ink to have an absorption coefficient (μ_a) of 0.15cm^{-1} and a reduced scattering coefficient (μ_s') of 10cm^{-1} at 650nm, according to [32]. The phantom contains several 5mm diameter hollow channels that pass through the block at various locations. Solid cylindrical inclusions of the same material, but with higher absorption (μ_a = 0.75cm^{-1}, μ_s' = 10cm^{-1} at 650nm), were placed in the hollow channels in different configurations. The remaining channels were filled with solid rods of the same optical properties as the block.

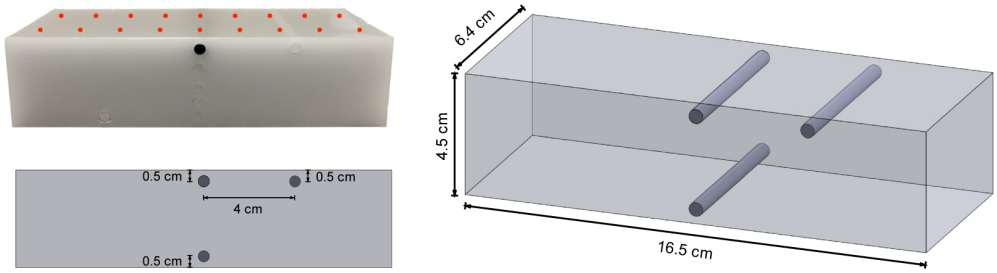

Fig. 8. Block phantom setup.

The phantom was imaged with and without the 5x higher absorbing inclusions using 18 source illumination positions (as depicted as red dots in Fig. 8), a 55ms integration time, and an EM gain setting of 5. A total of 32,154 pixel detectors were used to reconstruct a μ_a-map of the block phantom on a 126,048 tetrahedron volume mesh.

The system performance was evaluated using two different configurations shown in Fig. 9(a). Experimental results (Fig. 9(c)) were also compared against numerical simulations (Fig. 9(b)) of the digital phantom that uses the same geometry and optical properties as the block phantom. The reconstruction accuracy in terms of correlation (ρ) and deviation (δ) factors for each configuration are given in Table 2.

Biomedical Optics EXPRESS

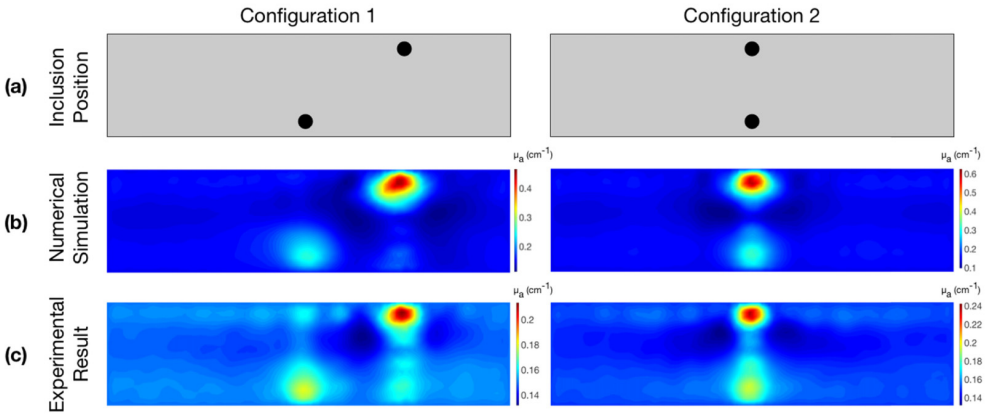

Fig. 9. Block phantom results with solid 5x absorbing inclusions in two configurations: (a) target, (b) numerical simulations, (c) experimental results.

Table 2. Quality of Block Phantom Reconstructions.

	$\overline{CD}$	$\overline{DE}$	$\overline{AO}$	$\overline{BO}$	α	β	ε	γ
	4.5 in.	2 in.	4 in.	7 in.	68º	27º	18º	81.9º

As given in Table 2, the experimental results agree well with the numerical simulations in the differentiation between inclusions at different locations, while the reconstructed contrasts of the inclusions are lower than those of the numerical simulations. To further evaluate performance, we also investigated the sensitivity of the system to resolve different target-to-background absorption contrasts. In the previous study, the hollow channels in the phantom were fitted with inclusions made of the same silicone material as the block and with the same reduced scattering coefficient. Here, in order to fabricate different absorption contrasts, the hollow channels were fitted with clear nylon tubing with 1/16in thick walls. The tubing was filled with 4 different ink contrasts (2x: $\mu_a = 0.3\text{cm}^{-1}$, 3x: $\mu_a = 0.45\text{cm}^{-1}$, 4x: $\mu_a = 0.6\text{cm}^{-1}$, and 5x: $\mu_a = 0.75\text{cm}^{-1}$) in the same configurations as Fig. 9(a). The results are shown in Fig. 10. The recovered contrast was calculated from the max μ_a and the mean background μ_a for the top and bottom inclusions separately and plotted versus the target contrast.

In all four cases with varying absorption contrasts, the system performs well at localizing the target inclusions. Overall, the quantitative recovery of the absorption coefficient was underestimated as similarly observed in Fig. 9. This is a well-known phenomenon in DOT. Furthermore, the inclusions at the top of the phantom were consistently reconstructed with higher values than the inclusions at the bottom of the phantom. This is expected since the sensitivity at the top surface is higher than at the bottom. This is due to the source positions only being applied to the top surface, while detectors are utilized both from the top and bottom surfaces. This was already confirmed in the numerical simulations in Fig. 9(b). Despite the underestimation of the absorption coefficient, the recovered contrast increases with increasing target contrast. This demonstrates the system's ability to detect relative changes in absorption.

Biomedical Optics EXPRESS

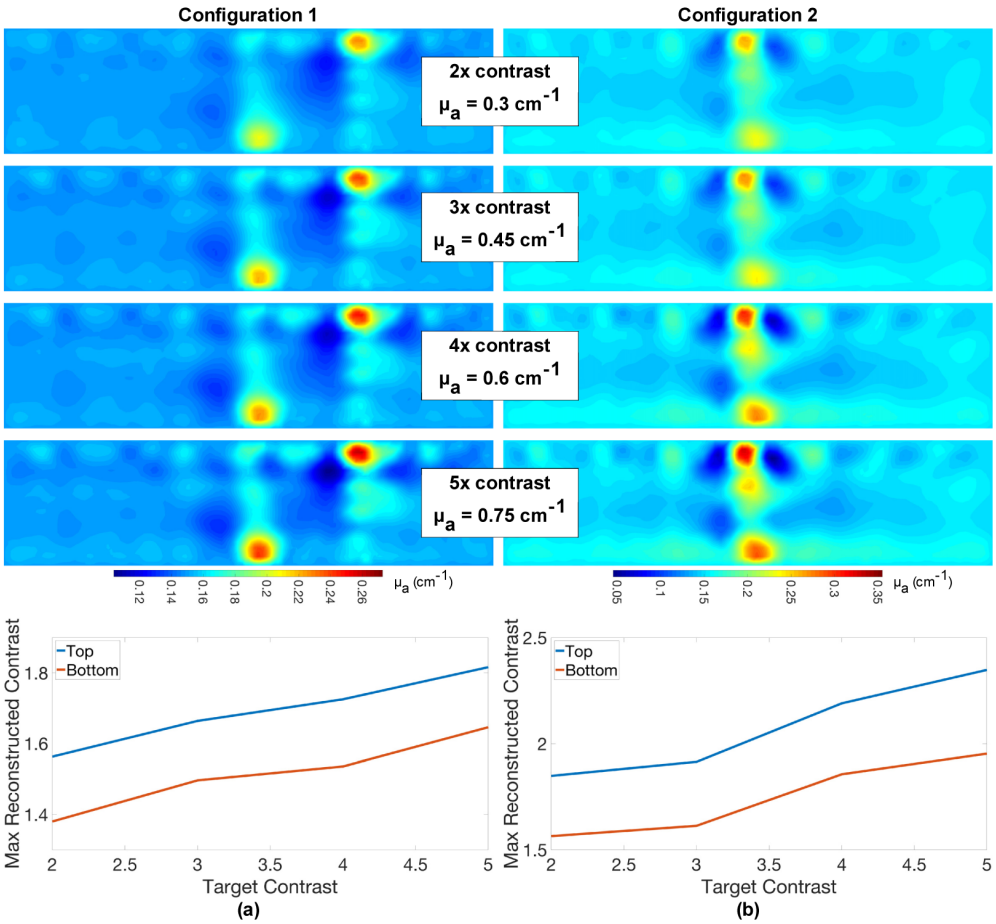

Fig. 10. Block phantom results with inclusions at 2x-5x contrast in (a) Configuration 1 and (b) Configuration 2 with the max recovered contrast plotted against the actual target contrast.

4.6 Foot phantom experiments

A silicone-based foot phantom, shown Fig. 11(a), was fabricated in a similar manner as the block phantom above. This foot phantom was used to test the system's ability to resolve more complex and realistic vascular systems such as those found at the mid-metatarsal level of the foot. Three different water-soluble channel systems were 3D printed and inserted into a foot mold. These channel systems mimic the vasculature in the three angiosomes in the distal portion of the foot: dorsalis pedis artery (DPA), medial plantar artery (MPA), and lateral plantar artery (LPA) angiosomes. They start as three main arteries and branch into eight vessels at the mid-metatarsal level, as detailed in Fig. 11(b, c). After the PDMS cured around the vascular network, the network was dissolved leaving open channels. The channels can be filled independently with liquid solutions of varying optical properties.

Three combinations of the angiosome channels were filled with dilutions of India Ink while the remaining angiosome channels were filled with water. These cases were imaged with 20 source positions (as shown in Fig. 12(d)), a 50ms integration time, and an EM gain setting of 5. A total of 19,633 pixel detectors were used to reconstruct a μ_a-map on a 39,167 tetrahedron volume mesh. The results of the reconstructions are shown in Fig. 12(a-c).

Biomedical Optics EXPRESS

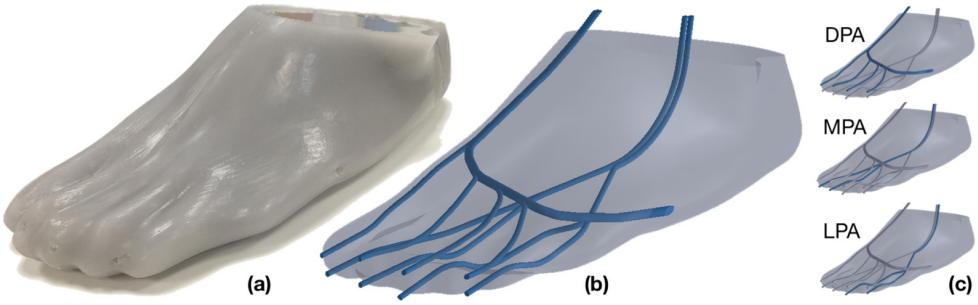

Fig. 11. Foot phantom setup: (a) Image of the foot phantom with 20 source positions. (b) Model of the foot phantom vessel. (c) Detailed depictions of each vessel structure representing the three angiosomes.

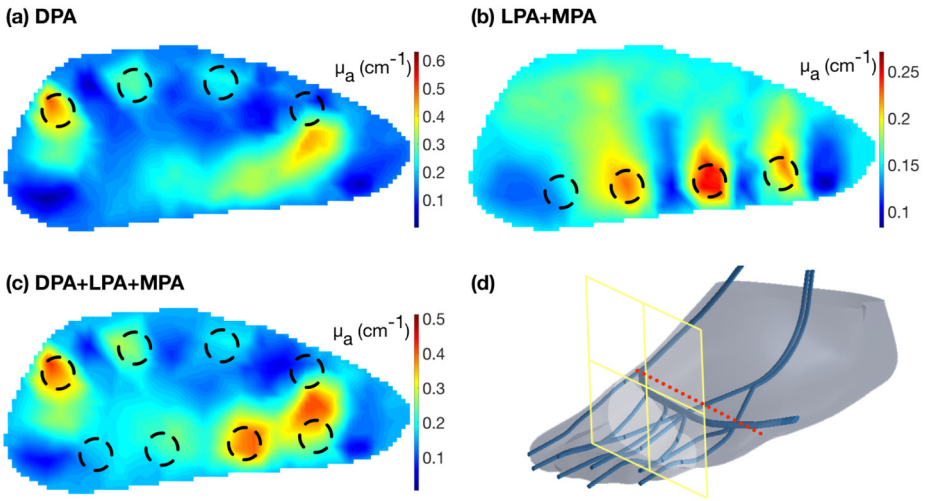

Fig. 12. (a-c) Foot phantom results for three inclusion combinations, where black dotted circles represent the expected area of the inclusion. (d) The source positions used and approximate cross–section depicted in (a-c).

Although the exact locations of the channels are not known, the black dashed circles represent the general expected location of the vessels within the foot phantom, which show a reasonable agreement with the reconstruction result in most cases. For example, in the cases where the bottom channels have higher absorption (Fig. 12 (b, c)), the reconstructions show good agreement with the expected locations at the bottom of the foot. However, the absorption for the MPA channels on the bottom left is not as high as the LPA channels on the bottom right in Fig. 12(c). This is due to a leak that developed in the MPA channels prior to imaging for the configuration in Fig. 12(c).

In the cases where the DPA channels have higher absorption (Fig. 12(a, c)), there is a relatively higher absorption close to the expected areas. The lateral channel on the right is not resolved separately from the LPA channel on the bottom. This reveals a limitation of the system in resolving depth in the thinner area of the foot.

Furthermore, the two center channels also have lower reconstructed absorption compared to the outer channels. This may be due to the size by the differences in the channel diameters and the uncertainty in the channel positions. The inflow and outflow channels of the DPA angiosome (represented by the upper left and upper right circles, respectively) have larger diameters than the 4 vessels branching off from the arch. In addition, a single line of source positions was used in this experiment, which may have been positioned right above or behind

Biomedical Optics EXPRESS

the major arch of DPA channel arch. The single line of sources decreased the resolution along the length of the foot. Depending on this line of sources exact position relative to the vessel structure, the detection sensitivity to the DPA vessel structure changes. We suspect that in this specific setup, we had the highest sensitivity just behind the arch. At this cross section, the larger inflow and outflow vessels are detected with a high sensitivity while the smaller branched vessels are detected with a lower sensitivity. Despite these limitations, the results demonstrate a reasonable ability to localize the inclusions at the general expected areas. Future studies with an improved foot phantom will involve dynamic studies involving varying concentrations of ink and increased source resolution along the length of the foot.

4.7 In vivo healthy foot experiment

We have previously shown that DDOT can distinguish between healthy and affected vasculature by measuring the hemodynamics in the foot during a venous occlusion [11, 12]. As an initial test and proof-of-concept of this system, we imaged a healthy foot during a venous occlusion and qualitatively evaluated the results. The venous occlusion is achieved by inflating a pressure cuff at the thigh to ≥60mmHg. During the occlusion, venous outflow from the extremity is blocked while arterial inflow is left intact such that there is an accumulation of blood in the foot during the occlusion. Time-dependent features of this accumulation reveal information regarding the arterial vasculature in the lower extremity and the perfusion of blood in the foot.

The left foot of a healthy volunteer was imaged for approximately 40 seconds of baseline, 90 seconds of venous occlusion at 80mmHg, and 50 seconds of recovery. The images were acquired at approximately 0.33Hz using 10 source illumination positions in a single line across the foot, a 75ms integration time, and an EM gain factor of 50. A total of 22,554 pixel detectors were used to reconstruct the relative change in [Hb] and [HbO_2] on a 59,883 tetrahedron foot volume mesh. The reference concentrations of [Hb] and [HbO_2] were assumed to be 14.69μM and 23.43μM, respectively. The final reconstruction of the previous frame was used as the initial guess for the reconstruction of the next frame. Figure 13(a) shows 2D cross sectional maps of the change in total hemoglobin Δ[HbT] at relevant time points before, during, and after the occlusion. The spatial maps show areas of high Δ[HbT] at the top and bottom of the foot during the venous occlusion. These regions can be attributed to areas in the foot with vasculature and correlate with expected areas of perfusion.

To track the time course of the Δ[HbT] in these areas, we used a correlation coefficient method to define the vascular region of interest (ROI) in the foot (as in our previous study [11]). Specifically, the mean Δ[HbT] over the entire volume of the foot is calculated for each time point to produce a time trace of the volume average Δ[HbT] within the foot. Similar time traces for each individual volume element are compared to the volume average Δ[HbT] by calculating the correlation coefficient. ROIs that represent the vascular areas of the foot were defined as volume elements with a correlation coefficient >0.65. The ROIs were further segmented into the three angiosome regions. The mean Δ[HbT] within the ROIs of each angiosome is plotted over time in Fig. 13(b), with the DPA shown in blue, the MPA shown in orange, and the LPA shown in green.

Biomedical Optics EXPRESS

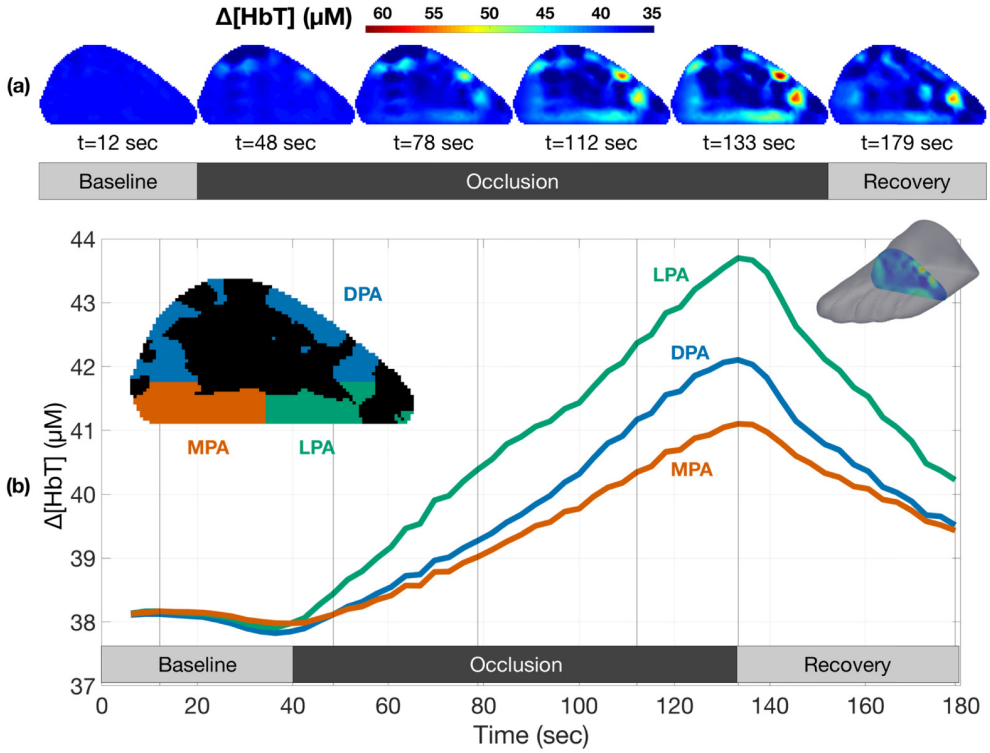

Fig. 13. Reconstruction results of an in vivo healthy foot during a venous occlusion. (a) 2D spatial maps of total hemoglobin concentration [HbT]. (b) Time traces of the average [HbT] change in regions of interest within the three angiosomes.

This experiment was repeated on the same foot on a second day and compared to the initial experiment to test the in vivo repeatability of the system. The resulting spatial maps and time traces matched the initial experiment well. The 2D spatial maps of Δ[HbT] at the end of the venous occlusion had a high correlation factor ρ of 0.9967, and a low deviation factor δ of 0.1117 for the two days (Fig. 14). The extracted time traces also had a high correlation factor ρ >0.997 for each angiosome, indicating that the perfusion values are similar for different days. However, slight differences between days could be attributed to physiological differences arising from natural day-to-day differences. This will be the subject of future studies.

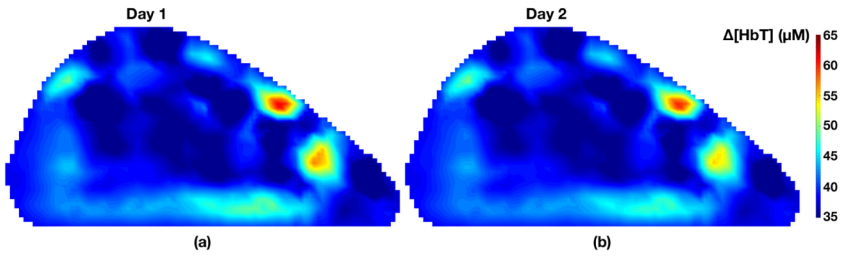

Fig. 14. 2D spatial maps of Δ[HbT] at the end of the venous occlusion on (a) day 1 and (b) day 2, showing very similar regions of blood perfusion.

Overall, the 2D maps of the Δ[HbT] reveal regions of interest at the top and bottom of the foot that match the vascular areas at the mid-metatarsal level of the foot. The extracted time traces of Δ[HbT] from those regions of interest also match the expected trends from previous

Biomedical Optics EXPRESS

work. These measurements are an initial demonstration of the system's ability to reliably make in vivo measurements of hemodynamic changes within the foot during a venous occlusion.

5. Summary

In this work, we developed a novel multi-view contact-free DDOT system to image hemodynamics in the foot, which may be useful in evaluating PAD in the future. The measurement operator allows reconstruction of non-contact data from multiple surfaces simultaneously. This enables the upright design of the system, a form factor that is small enough to be easily moved and stored in the clinical setting. In addition, the fiber-less tissue interface reduces the setup time and avoids issues common with fiber-based DDOT systems. The resulting system is suitable for the clinical setting and for patients with open wounds and ulcers.

We presented the design and implementation of our DDOT system for imaging tissue perfusion in the foot. We characterized and experimentally validated the system on tissue-mimicking phantoms and demonstrated its ability to localize and quantify relative changes in absorption. This is important in dynamic studies where time-dependent changes are used instead of absolute concentrations. Finally, repeated in vivo tests in a healthy foot demonstrate the potential of the system to evaluate the vasculature in the lower extremities by measuring the perfusion in the foot during a venous occlusion at 0.33Hz. The frame-rate can be increased by utilizing less sources, or shorter integration times and additional EM gain.

The main advantages of this system are its non-contact and multi-view capabilities. By designing and implementing this system, we have facilitated further investigation of PAD, especially in patients with open wounds, which are difficult to evaluate with fiber-based contact systems. This new system provides a functional measure of the perfusion in the foot, which fills a gap in the current clinical evaluation tools for PAD. For example, this system may prove useful in revealing under-perfused angiosomes within the foot and informing revascularization procedures. In addition, we may gain a better understanding of the link between blood perfusion and wound healing with future studies. This system can also be generalized to imaging other tissues, the hand and fingers in rheumatoid arthritis, for example.

Funding

National Heart, Blood, and Lung Institute (NHLBI- 1R01-HL115336); Wallace H. Coulter Foundation (WHCF CU11-2443); BioAccelerate New York City Partnership Fund.

Acknowledgments

The authors thank Jong Hwan Lee for his assistance and support throughout this work. Furthermore, we would like to thank Dr. Danielle R. Bajakian, MD, from the Dept. of Surgery, Division of Vascular Surgery and Endovascular Interventions, at Columbia University Medical Center, for her insights concerning lower extremity vasculature.

Disclosures

JWH: (P). HKK: (P). CJF: (P). AHH: (P).

References

1. J. E. Gunther, E. A. Lim, H. K. Kim, M. Flexman, M. Altoé, J. A. Campbell, H. Hibshoosh, K. D. Crew, K. Kalinsky, D. L. Hershman, and A. H. Hielscher, "Dynamic diffuse optical tomography for monitoring neoadjuvant chemotherapy in patients with breast cancer," Radiology **287**(3), 778–786 (2018).
2. B. J. Tromberg, B. W. Pogue, K. D. Paulsen, A. G. Yodh, D. A. Boas, and A. E. Cerussi, "Assessing the future of diffuse optical imaging technologies for breast cancer management," Med. Phys. **35**(6), 2443–2451 (2008).
3. B. J. Tromberg, Z. Zhang, A. Leproux, T. D. O'Sullivan, A. E. Cerussi, P. M. Carpenter, R. S. Mehta, D. Roblyer, W. Yang, K. D. Paulsen, B. W. Pogue, S. Jiang, P. A. Kaufman, A. G. Yodh, S. H. Chung, M. Schnall,

Biomedical Optics EXPRESS

B. S. Snyder, N. Hylton, D. A. Boas, S. A. Carp, S. J. Isakoff, and D. Mankoff; ACRIN 6691 investigators, "Predicting responses to neoadjuvant chemotherapy in breast cancer: acrin 6691 trial of diffuse optical spectroscopic imaging," Cancer Res. **76**(20), 5933–5944 (2016).
4. C. Xu, H. Vavadi, A. Merkulov, H. Li, M. Erfanzadeh, A. Mostafa, Y. Gong, H. Salehi, S. Tannenbaum, and Q. Zhu, "Ultrasound-guided diffuse optical tomography for predicting and monitoring neoadjuvant chemotherapy of breast cancers: recent progress," Ultrason. Imaging **38**(1), 5–18 (2016).
5. M. G. Pakalniskis, W. A. Wells, M. C. Schwab, H. M. Froehlich, S. Jiang, Z. Li, T. D. Tosteson, S. P. Poplack, P. A. Kaufman, B. W. Pogue, and K. D. Paulsen, "Tumor angiogenesis change estimated by using diffuse optical spectroscopic tomography: demonstrated correlation in women undergoing neoadjuvant chemotherapy for invasive breast cancer?" Radiology **259**(2), 365–374 (2011).
6. A. H. Hielscher, H. K. Kim, L. D. Montejo, S. Blaschke, U. J. Netz, P. A. Zwaka, G. Illing, G. A. Muller, and J. Beuthan, "Frequency-domain optical tomographic imaging of arthritic finger joints," IEEE Trans. Med. Imaging **30**(10), 1725–1736 (2011).
7. H. Y. Wu, A. Filer, I. Styles, and H. Dehghani, "Development of a multi-wavelength diffuse optical tomography system for early diagnosis of rheumatoid arthritis: simulation, phantoms and healthy human studies," Biomed. Opt. Express **7**(11), 4769–4786 (2016).
8. L. Xi and H. Jiang, "Integrated photoacoustic and diffuse optical tomography system for imaging of human finger joints in vivo," J. Biophotonics **9**(3), 213–217 (2016).
9. C. L. Evans, "Peering inside the mind: Imaging brain activity with advanced diffuse optical tomography," Sci. Transl. Med. **8**(360), 360ec162 (2016).
10. C. W. Lee, R. J. Cooper, and T. Austin, "Diffuse optical tomography to investigate the newborn brain," Pediatr. Res. **82**(3), 376–386 (2017).
11. M. A. Khalil, H. K. Kim, J. W. Hoi, I. Kim, R. Dayal, G. Shrikhande, and A. H. Hielscher, "Detection of peripheral arterial disease within the foot using vascular optical tomographic imaging: a clinical pilot study," Eur. J. Vasc. Endovasc. Surg. **49**(1), 83–89 (2015).
12. M. A. Khalil, H. K. Kim, I. K. Kim, M. Flexman, R. Dayal, G. Shrikhande, and A. H. Hielscher, "Dynamic diffuse optical tomography imaging of peripheral arterial disease," Biomed. Opt. Express **3**(9), 2288–2298 (2012).
13. R. P. Boezeman, F. L. Moll, Ç. Ünlü, and J. P. de Vries, "Systematic review of clinical applications of monitoring muscle tissue oxygenation with near-infrared spectroscopy in vascular disease," Microvasc. Res. **104**, 11–22 (2016).
14. M. D. Gerhard-Herman, H. L. Gornik, C. Barrett, N. R. Barshes, M. A. Corriere, D. E. Drachman, L. A. Fleisher, F. G. Fowkes, N. M. Hamburg, S. Kinlay, R. Lookstein, S. Misra, L. Mureebe, J. W. Olin, R. A. Patel, J. G. Regensteiner, A. Schanzer, M. H. Shishehbor, K. J. Stewart, D. Treat-Jacobson, and M. E. Walsh, "2016 AHA/ACC Guideline on the Management of Patients With Lower Extremity Peripheral Artery Disease: A Report of the American College of Cardiology/American Heart Association Task Force on Clinical Practice Guidelines," Circulation **135**(12), e726–e779 (2017).
15. M. H. Shishehbor, T. A. Hammad, T. Zeller, I. Baumgartner, D. Scheinert, and K. J. Rocha-Singh, "An analysis of IN.PACT DEEP randomized trial on the limitations of the societal guidelines-recommended hemodynamic parameters to diagnose critical limb ischemia," J. Vasc. Surg. **63**(5), 1311–1317 (2016).
16. A. Krnic, N. Vucic, and Z. Sucic, "Duplex scanning compared with intra-arterial angiography in diagnosing peripheral arterial disease: three analytical approaches," Vasa **35**(2), 86–91 (2006).
17. A. W. Pollak, P. T. Norton, and C. M. Kramer, "Multimodality imaging of lower extremity peripheral arterial disease: current role and future directions," Circ Cardiovasc Imaging **5**(6), 797–807 (2012).
18. S. Novo, "Classification, epidemiology, risk factors, and natural history of peripheral arterial disease," Diabetes Obes. Metab. **4**(s2 Suppl 2), S1–S6 (2002).
19. C. E. Attinger, K. K. Evans, E. Bulan, P. Blume, and P. Cooper, "Angiosomes of the foot and ankle and clinical implications for limb salvage: reconstruction, incisions, and revascularization," Plast. Reconstr. Surg. **117**(7 Suppl), 261S–293S (2006).
20. H. Jongsma, J. A. Bekken, G. P. Akkersdijk, S. E. Hoeks, H. J. Verhagen, and B. Fioole, "Angiosome-directed revascularization in patients with critical limb ischemia," J. Vasc Surg **65**, 1208–1219 (2017).
21. M. C. Bunte and M. H. Shishehbor, "Angiosome-guided intervention in critical limb ischemia," Interv. Cardiol. Clin. **6**(2), 271–277 (2017).
22. T. Y. Huang, T. S. Huang, Y. C. Wang, P. F. Huang, H. C. Yu, and C. H. Yeh, "Direct revascularization with the angiosome concept for lower limb ischemia: a systematic review and meta-analysis," Medicine (Baltimore) **94**(34), e1427 (2015).
23. J. A. Guggenheim, H. R. Basevi, J. Frampton, I. B. Styles, and H. Dehghani, "Multi-modal molecular diffuse optical tomography system for small animal imaging," Meas. Sci. Technol. **24**(10), 105405 (2013).
24. J. H. Lee, H. K. Kim, C. Chandhanayingyong, F. Y. I. Lee, and A. H. Hielscher, "Non-contact small animal fluorescence imaging system for simultaneous multi-directional angular-dependent data acquisition," Biomed. Opt. Express **5**(7), 2301–2316 (2014).
25. M. F. Chen, Y. P. Chen, and W. T. Hsiao, "Correction of field distortion of laser marking systems using surface compensation function," Opt. Lasers Eng. **47**(1), 84–89 (2009).
26. Y. Li, "Beam deflection and scanning by two-mirror and two-axis systems of different architectures: a unified approach," Appl. Opt. **47**(32), 5976–5985 (2008).

Biomedical Optics EXPRESS

27. A. Manakov, H.-P. Seidel, and I. Ihrke, *A Mathematical Model and Calibration Procedure for Galvanometric Laser Scanning Systems* (2011), pp. 207–214.
28. J. Jia, J. Lee, L. D. Montejo, H. K. Kim, and A. H. Hielscher, "Measurement operator for angular dependent photon propagation in contact-free optical tomography," Proc. SPIE **8578**, 857815 (2013).
29. H. K. Kim, M. Flexman, D. J. Yamashiro, J. J. Kandel, and A. H. Hielscher, "PDE-constrained multispectral imaging of tissue chromophores with the equation of radiative transfer," Biomed. Opt. Express **1**(3), 812–824 (2010).
30. H. K. Kim and A. H. Hielscher, "A PDE-constrained SQP algorithm for optical tomography based on the frequency-domain equation of radiative transfer," Inverse Probl. **25**(1), 015010 (2009).
31. H. K. Kim, J. Gunther, J. Hoi, and A. H. Hielscher, "A reduced-space basis function neural network method for diffuse optical tomography," Proc. SPIE **8578**, 857815 (2015).
32. F. Ayers, A. Grant, D. Kuo, D. J. Cuccia, and A. J. Durkin, "Fabrication and characterization of silicone-based tissue phantoms with tunable optical properties in the visible and near infrared domain," Proc. SPIE **6870**, 687007 (2008).